Nonlinear XY and p-clock models on sparse random graphs: Mode-locking transition of localized waves

Alessia Marruzzo and Luca Leuzzi*

Department of Physics, Sapienza Università di Roma, Piazzale Aldo Moro 2, I-00185 Rome, Italy
and IMIP-CNR, Rome Unit Kerberos, Piazzale Aldo Moro 2, I-00185 Rome, Italy

(Received 21 November 2014; revised manuscript received 30 January 2015; published 17 February 2015)

A statistical mechanic study of the XY model with nonlinear interaction is presented on bipartite sparse random graphs. The model properties are compared to those of the p-clock model, in which planar continuous spins are discretized into p values. We test the goodness of the discrete approximation to XY spins used in numerical computations and simulations and its limits of convergence in given, p-dependent temperature regimes. The models are applied to describe the mode-locking transition of the phases of light modes in lasers at the critical lasing threshold. A frequency is assigned to each variable node, and function nodes implement a frequency matching condition. A nontrivial unmagnetized phase-locking occurs at the phase transition, where the frequency dependence of the phases turns out to be linear over a broad range of frequencies, as in a standard mode-locking multimode laser at the optical power threshold.

DOI: 10.1103/PhysRevB.91.054201 PACS number(s): 05.70.Fh, 42.60.Fc, 42.65.Sf, 75.10.Hk

I. INTRODUCTION

The XY model with linearly interacting spins is well known in statistical mechanics, displaying important physical insights and applications, starting from the Kosterlitz-Thouless transition in two dimensions [1] and moving to, e.g., the transition of liquid helium to its superfluid state [2,3], the roughening transition of the interface of a crystal in equilibrium with its vapor [4], or synchronization problems related to the Kuramoto model [5–7]. Furthermore, the XY model with nonlinear interaction terms has been used to investigate the topological properties of potential energy landscapes in configuration space [8]. Our motivations to study nonlinear XY models are, however, to be found in optics, to describe, e.g., the nonlinear interaction among electromagnetic modes in a laser cavity [9–11], as well as the lasing transition in cavityless amplifying resonating systems in random media known as *random lasers* [12–15]. Stimulated by this recent cross-fertilization of the fields of statistical mechanics and laser optics, we analyze a diluted four-body interacting XY model on sparse random graphs including mode frequencies and gain profiles.

Due to the absence of the cavity, the mode profiles in random lasers cannot be determined as solutions of the Helmholtz equation. Moreover, light scatterers (acting as gain material [16]) are usually randomly distributed inside the systems and the modes are more localized with respect to ordinary lasers, where each mode extends over the whole cavity. In order to interact nonlinearly, the modes need to spatially overlap. Therefore, the effects of dilution are certainly relevant. More in general, sparse random graphs can be used in the study of interference effects among neighborhood modes in light guides [17]. This type of topology is also of interest in designed experiments of interactions among modes of apart lasers [18–20]. In order to understand the possible effects of disorder in the degree of the connectivity of each mode, we, furthermore, consider the cases of both constant and random Poisson-distributed connectivity [i.e., Bethe and Erdòs-Rényi (ER)].

Mode- or *phase*-locking [21] consists in the amplification of very short pulses produced by the synchronization of the phases of longitudinal axial modes in the cavity. In the case of *passive* mode-locking (ML), yielding the shortest pulses, synchronization is due to nonlinear mode-coupling. The most effective known mechanism to induce nonlinearity is saturable absorption, that is, the selective absorption of low-intensity light and the transmission of high-intensity light, leading, after many cavity round-trips, to a stationary train of ultrashort pulses. Such pulses are composed of interacting modes of given, equispaced, frequencies ω around a central frequency ω_0. In the typical case of third-order nonlinearity, [21–23] the modes interact as quadruplets and must satisfy the frequency matching condition (FMC)

$$|\omega_j - \omega_k + \omega_l - \omega_m| \leqslant \gamma \tag{1}$$

for each quadruplet composed of modes (j,k,l,m), γ being the linewidth of the single mode. For such modes a constant *phase delay* occurs, i.e.,

$$\phi(\omega) \simeq \phi(\omega_0) + \phi' \times (\omega - \omega_0), \tag{2}$$

and the resulting electromagnetic signal is unchirped. Mode phases are, then, constrained as the relative frequencies by Eq. (1) and they are said to be *locked*. If, as in standard laser cavities, resonances are narrow and evenly spaced, phases will, thus, be evenly spaced as well. In lasers with a large-gain bandwidth, the progressive depletion of low-intensity wings of the light pulse traveling through the cavity in each round-trip causes the amplification of very short pulses composed of modes with locked phases.

When a laser operates in the multimode regime and reaches a stationary state driven by optical pumping, the interaction among the modes can be described by the effective four-mode interacting Hamiltonian [9,15,24]

$$\mathcal{H} = -\mathrm{Re}\left[\sum_k g_k a_k^* a_k + J \sum_{\{\omega_j,\omega_k,\omega_l,\omega_m\}}^{\mathrm{FMC}} a_j^* a_k a_l^* a_m\right], \tag{3}$$

*luca.leuzzi@cnr.it

where $a_j \equiv A_j e^{i\phi_j}$ is the complex amplitude of the light mode with eigenvector $\mathbf{E}_j(\mathbf{r})$, the coefficient of the following expansion for the electromagnetic field:

$$\mathbf{E}(\mathbf{r},t) = \sum_j a_j(t)\mathbf{E}_j(\mathbf{r})e^{-i\omega_j t} + \text{c.c.} \tag{4}$$

In the statistical mechanic approach, the total optical power pumped into the system is required to be a constant of the problem, i.e., the system is in a stationary, pumping-driven regime effectively representable as equilibrium phases in an adequate ensemble. The total power is $\mathcal{E} = N\epsilon = \sum_k a_k a_k^*$. The linear local coefficient g_k in Eq. (3) is the net gain profile and the nonlinear coupling coefficient J represents the self-amplitude modulation coefficient of the saturable absorber responsible for the ML regime [23]. It can be expressed, as well, in terms of the spatial overlap of the eigenvectors [11], i.e., given any four modes (j,k,l,m),

$$J \propto \int d\boldsymbol{r}\, \hat{\chi}^{(3)}(\boldsymbol{r};\omega_j,\omega_k,\omega_l,\omega_m) \vdots \boldsymbol{E}_\mathbf{j}(\boldsymbol{r})\boldsymbol{E}_\mathbf{k}(\boldsymbol{r})\boldsymbol{E}_\mathbf{l}(\boldsymbol{r})\boldsymbol{E}_\mathbf{m}(\boldsymbol{r}), \tag{5}$$

where $\hat{\chi}^{(3)}$ is the nonlinear susceptibility tensor of the optically active medium.

We use the parameter β as the external driving force of the transition. In thermodynamic systems coupled to a thermal reservoir at temperature T, $\beta = 1/(k_B T)$ is simply the inverse temperature. In photonic systems it stands for an effective inverse temperature related to both the real heat-bath temperature T_{bath} of the optically active medium and the optical power ϵ pumped into the system as

$$\beta J \propto \frac{\epsilon^2 J}{k_B T_{\text{bath}}} \equiv \mathcal{P}^2, \tag{6}$$

where $\mathcal{P}$ is the so-called pumping rate [9,11,13,14].

The paper is organized as follows: in Sec. II we introduce the 4-XY and the 4-p-clock models; in Sec. III we recall the methods employed in the analysis of the model and determine belief propagation (BP) and cavity equations for the specific models; and in Secs. IV and V we present the results on Bethe and on ER graphs. Finally, in Sec. VI we introduce a tree-like ML network and study the transition between the phase-incoherent regime and the coherent mode-locked regime typical of ultrafast multimode lasers.

II. 4-XY MODEL AND 4-p-CLOCK MODEL

The dynamic time scales of magnitudes $\{A_j = |a_j|\}$ and phases $\{\phi_j = \arg(a_j)\}$ of the complex amplitudes are well separated. Since we are interested in studying the phase-locking transition, we can consider observing the system dynamics at a time scale longer than one of the phases but sensitively shorter than one of the magnitudes, thus regarding the amplitude magnitudes A_k as constants. Within this *quenched amplitude* approximation [12,13], from Eq. (3) we obtain

$$\mathcal{H} = -\sum_{jklm} J_{jklm}\cos(\phi_j - \phi_k + \phi_l - \phi_m), \tag{7}$$

where we have rescaled $JA_jA_kA_lA_m \to J_{jklm}$. The sum $\sum_{jklm}$ goes over the quadruplets for which the quenched coefficients J_{jklm} are different from 0, i.e., all quadruplets whose electromagnetic fields overlap in space and whose frequencies satisfy the FMC, Eq. (1). The Hamiltonian $\mathcal{H}$ is invariant under the SO(2) group, i.e., rotations in two dimensions. Imposing the further approximation that all amplitudes are quenched *and* equal to each other, i.e., there is intensity equipartition in every regime, one can define the ferromagnetic (FM) nonlinear 4-XY model, $J_{jklm} = J, \forall(j,k,l,m)$, whose behavior is presented in this work on specific interaction networks.

As stated in Sec. 1, we consider cases in which the number of interacting quadruplets per mode does not grow with the size of the system. In terms of the physical relationship between the interaction coefficient and the space localization of modes [cf. Eq. (5)], this corresponds to modes whose localization in space has an overall small volume but takes place in far-apart, even disjoint, regions, yielding a dilute, distance-independent interaction network. These diluted model instances are represented as bypartite graphs.

Besides the XY model, where spins are unitary vectors on a plane, $\boldsymbol{\sigma} \equiv (\cos\phi, \sin\phi)$, $\phi \in [0,2\pi)$, we consider a discretized version, where the phases ϕ can only take p values, equispaced in radiants by $2\pi/p$:

$$\phi_a = \frac{2\pi}{p}a; \quad a = 0,1,\ldots,p-1. \tag{8}$$

We use p even, in order to be able to extend to the antiferromagnetic and spin-glass cases, where the interactions among spins can also be negative. Indeed, if p is odd, it is not possible to find a discretization of the $[0,2\pi)$ interval in such a way as to allow the four interacting spins to find the most energetically favorable configurations for both $J > 0$ and $J < 0$. To better exemplify this, if $J < 0$, the minimal contribution of a single (1,2,3,4) quadruplet to the energy is such that $\phi_1 + \phi_2 = \phi_3 + \phi_4 + \pi$. Discretizing according to Eq. (8) this implies $a_1 + a_2 = p/2 + a_3 + a_4$, which is effective only if p is even.

The p-clock model can also be seen as a generalization of the Ising model from 2 to p possible states for the local magnetization σ_i: a spin varies over the p roots of unity $e^{2\pi a/p}$. The Hamiltonian, Eq. (7), is invariant under the discrete symmetry group Z_p, consisting of multiplying all the σ_i's by the same pth root. We know that in the Ising case two phases can coexist when the symmetry Z_2 is broken. In the $p > 2$ case, there are p phases that may coexist when the symmetry is broken. We use the p-clock model as an effectively tuned numerical representation for the XY model. Because the latter is a continuous model, we expect infinitesimal fluctuations with an infinitesimal energy cost to occur. These cannot be present in a discrete model at low temperatures: thus, it is only in the $p \to \infty$ limit that we expect to recover all results of the XY model also in the $\beta \to \infty$ limit. For finite β, however, to some extent the two representations coincide. In Secs. IV and V we quantitatively determine this extent.

Before presenting these results, in the next section we briefly recall the main tools used, i.e., BP, the cavity method (CM), and the population dynamics algorithm. The paper is organized in such a way that the reader already familiar with these algorithms can skip Sec. III and proceed to Sec. IV.

III. BELIEF PROPAGATION OF THE 4-XY MODEL ON FACTOR GRAPHS

We study the 4-XY model, Eq. (7), on sparse random graphs. In order to represent the four-body interaction of phase variables ϕ, we, thus, resort to the factor graph representation in terms of functional nodes of connectivity $k=4$ for interacting quadruplets and variable nodes of connectivity c for mode phases involved in c quadruplets. Let us label $m=1,\ldots,M$ the function nodes and ∂m the variable nodes connected to the function node m. The phase ϕ_i is the value of the variable node $i=1,\ldots,N$.

A generic factor graph will be schematically indicated by $G_N(k,M)$, where N is the number of variable nodes, M the number of function nodes (i.e., the number of interacting k-uples), Mk the number of edges connecting variable nodes to function nodes, and $\alpha=M/N=c/k$ the connectivity coefficient. In general, we are interested not only in single instances, $G_N(k,M)$, but also in an ensemble of factor graphs. We focus on two large general groups: random regular graphs, also known as Bethe lattices, and ER graphs. Bethe graphs are defined as follows: for each function node m the k-tuple ∂m is taken uniformly at random from all the $\binom{N}{k}$ possible ones. In this case the fixed degree of connectivity c of a variable node is

$$c=M\frac{\binom{N}{k-1}}{\binom{N}{k}}=\frac{Mk}{N-(k-1)}=\frac{Mk}{N}\left[1+\mathcal{O}\left(\frac{k}{N}\right)\right] \quad (9)$$

in the diluted graph $k\ll N$.

In ER graphs each k-tuple is added to the factor graph independently, with probability $N\alpha/\binom{N}{k}$. It can be proved [25] that the total number of function nodes is a random variable with expected value $\langle M\rangle=N\alpha$, while the degrees c_i of the variable nodes are, in the large-N limit, Poissonian independent identically distributed (i.i.d.) random variables with average $c=\langle c_i\rangle=\alpha k$.

The factor graph representation for systems described by Eq. (7) yields the following joint probability of a configuration of planar spins, i.e., phases $\boldsymbol{\phi}=(\phi_1,\phi_2,\ldots,\phi_N)$:

$$P(\boldsymbol{\phi})=\frac{1}{Z}\prod_{m=1}^{M}\psi_m(\phi_{\partial m}). \quad (10)$$

In order to find the equilibrium configurations of the system and study the thermodynamic properties, we will use the BP method for factor graphs, $G_N(k,M)$, and the equivalent CM for ensembles of random factor graphs. BP is an iterative message-passing algorithm whose basic variables are messages associated with directed edges. For each edge (i,m) there exist two messages, $\nu_{i\to m}^{(t)}$ and $\hat{\nu}_{m\to i}^{(t)}$, that are updated iteratively in t as

$$\hat{\nu}_{m\to i}^{(t)}(\phi)=\frac{1}{z_{\text{test}}}\int_0^{2\pi}\prod_{j_l\in\partial m\setminus i}^{l=1,k-1}d\phi_{j_l}\nu_{j_l\to m}^{(t-1)}(\phi_{j_l}) \times\psi_m(\phi_{j_1},\ldots,\phi_{j_{k-1}},\phi), \quad (11)$$

$$\nu_{i\to m}^{(t)}(\phi)=\frac{1}{z_{\text{cav}}}\prod_{n\in\partial i\setminus m}\hat{\nu}_{n\to i}^{(t)}(\phi), \quad (12)$$

where $\partial m=\{j_1,j_2,j_3,i\}$, $\partial m\setminus i=\{j_1,j_2,j_3\}$, ∂i indicates the neighbor function nodes to variable node i, and $\partial i\setminus m$ are the function nodes connected to i but not m. z_{test} and z_{cav} are normalization factors. In the present XY model, Eq. (7), in which $k=4$, the Boltzmann weight function is

$$\psi_m(\phi_{j_1},\phi_{j_2},\phi_{j_3},\phi)=e^{\beta J\cos(\phi_{j_1}-\phi_{j_2}+\phi_{j_3}-\phi)}. \quad (13)$$

If the variable node i is at one end leaf of the graph, i.e., if $\partial i\setminus m$ is the empty set, then the uniform distribution holds, $\nu_{i\to m}(\phi)=1/(2\pi)$.[1] BP equations are exact on tree-like factor graphs. When all message marginals, $\{\nu_{i\to m},\hat{\nu}_{m\to i}\}$, are known, we can evaluate the marginal probability distributions of the variable nodes:

$$\mu_i(\phi_i)=\frac{1}{Z}\prod_{m\in\partial_i}\hat{\nu}_{m\to i}(\phi_i). \quad (14)$$

The free energy of the system reads [25]

$$F=\sum_{m=1}^{M}F_m+\sum_{i=1}^{N}F_i-\sum_{im\in E}F_{im}, \quad (15)$$

where E indicates the set of all edges in the graph and

$$F_m=-\frac{1}{\beta}\log\int_0^{2\pi}\prod_{i\in\partial m}d\phi_i\,\nu_{i\to m}(\phi_i)\psi_m(\phi_{\partial m}), \quad (16)$$

$$F_i=-\frac{1}{\beta}\log\int_0^{2\pi}d\phi_i\prod_{m\in\partial i}\hat{\nu}_{m\to i}(\phi_i), \quad (17)$$

$$F_{im}=-\frac{1}{\beta}\log\int_0^{2\pi}d\phi_i\,\hat{\nu}_{m\to i}(\phi_i)\nu_{i\to m}(\phi_i). \quad (18)$$

When we turn to ensembles of random factor graphs, the messages $\nu_{i\to m}\,(\hat{\nu}_{m\to i})$ become random variables: the idea is then to use BP equations to characterize their distributions in the large-N limit. Though BP equations are exact only in tree-graphical models and sources of errors can come from the existence of loops, they turn out to be a powerful tool in random graphs, as well. It is then useful to recall the results on the probability of loop occurrence and their average length in Bethe and ER graphs. It can be proved [25] that, if $\alpha k(k-1)<1$, the fraction of nodes in finite-size trees goes to 1 as the total number of nodes N goes to ∞: the probability of having loops of any size goes to 0. In the opposite case, $\alpha k(k-1)>1$, what is known as the "giant component" appears in the graph: a connected part containing many loops. Unlike the previous case, all the variable nodes almost surely belong to this connected component. However, in the diluted case, loops have infinite length and graphs look locally like trees.

BP being a local algorithm, one expects that, under the assumptions that correlations among variables go to 0 as the distance between them diverges, a property termed *clustering* [26], BP can be used to predict properties of the system in the thermodynamic limit. Then, for the case of random factor graphs, Eqs. (11) and (12) turn into equalities among the

[1]The effects of some external boundary can be described through the messages coming from the leaves. For example, if we want to consider a small external magnetic field, the $\nu_{i\to m}$ will depart from uniformity on the external shell of nodes.

distributions $P(\nu)$, $Q(\hat{\nu})$ of the messages, i.e.,

$$\hat{\nu}(\phi) \stackrel{d}{=} \frac{1}{z_{\text{test}}} \int_0^{2\pi} \prod_{l=1}^{k-1} d\phi_l \nu^l(\phi_l) \psi(\phi_1, \ldots, \phi_{k-1}, \phi), \quad (19)$$

$$\nu(\phi) \stackrel{d}{=} \frac{1}{z_{\text{cav}}} \prod_{m=1}^{c-1} \hat{\nu}^m(\phi), \quad (20)$$

where ν^l and are $\hat{\nu}^m$ are i.i.d. marginal functions and the connectivities k and c can, in principle, be random variables. The CM operates under the same assumptions we have outlined above but it supposes as well that Eqs. (19) and (20) have fixed-point solutions $\{P^*(\nu), Q^*(\hat{\nu})\}$ [27]. Focusing on these solutions, it evaluates recursively the partition functions by adding one variable at a time. In fact, the term "cavity" comes from the idea of creating a cavity around a variable by deleting one edge coming from that variable. For example, consider a random graph G where all edges coming from one constraint m have been erased; call $Z_{j\to m}(\phi_j)$ the partition function of one of the k-tree graphs starting from one of the $j \in \partial m$ with variable j fixed to ϕ_j. $Z_{j\to m}(\phi_j)$ can be computed recursively:

$$Z_{j\to m}(\phi_j) = \prod_{n\in\partial j\setminus m} \left[\prod_{i\in\partial n\setminus j} \int_0^{2\pi} d\phi_i \psi_n(\phi_{\partial n}) \times \prod_{i\in\partial n\setminus j} Z_{i\to n}(\phi_i) \right]. \quad (21)$$

BP equations, (11) and (12) are, then, obtained knowing the relation between BP messages and the partition function:

$$\nu_{j\to m} = \frac{Z_{j\to m}(\phi_j)}{\int_0^{2\pi} d\phi_j Z_{j\to m}(\phi_j)}.$$

Once the distributions of ν and $\hat{\nu}$ are known, the expected free energy per variable F/N can be computed taking the mean value of Eq. (15),

$$f = f_\nu + \frac{\bar{c}}{k} f_{\hat{\nu}} - \bar{c} f_{\nu\hat{\nu}}, \quad (22)$$

where

$$f_\nu = -\frac{1}{\beta} \mathbb{E}_{c,\{\hat{\nu}\}} \left[\log \int_0^{2\pi} d\phi \prod_{m=1}^{c} \hat{\nu}^m(\phi) \right],$$

$$f_{\hat{\nu}} = -\frac{1}{\beta} \mathbb{E}_{\{\nu\}} \left[\log \prod_{l=1}^{k} \int_0^{2\pi} d\phi_l \nu_l(\phi_l) \psi\left(\nu^1, \ldots, \nu^k\right) \right],$$

$$f_{\nu,\hat{\nu}} = -\frac{1}{\beta} \mathbb{E}_{\{\nu\},\{\hat{\nu}\}} \left[\log \int_0^{2\pi} d\phi \nu(\phi) \hat{\nu}(\phi) \right],$$

$\mathbb{E}$ indicates the expectation value with respect to the variables in the subscript, and $\bar{c}$ is the mean connectivity of variable nodes. Carrying out a functional derivative of Eq. (22), one can show that the stationary points of the free energy f are in one-to-one correspondence with solutions of BP equations.

The numerical method we use to solve Eqs. (19) and (20) is known in statistical physics as the population dynamics algorithm. The idea is to approximate the distributions $P(\nu)$ and $Q(\hat{\nu})$, through N i.i.d. copies of ν and $\hat{\nu}$. We call the sample $\{\nu_1, \ldots, \nu_N\}$ (same for $\hat{\nu}$) a population. Starting from an initial distribution, $\{\nu_1^0, \ldots, \nu_N^0\}$, as the population evolves and its size is large enough, the distributions will converge to the fixed-point solution $\{P^*(\nu), Q^*(\hat{\nu})\}$. The convergence of the algorithm is verified by evaluating the statistical fluctuations of intensive quantities. Fluctuations of order $1/\sqrt{N}$ indicate the convergence of the population to $\{P^*, Q^*\}$ [25]. Note that, for random regular graphs, since the connectivity is the same for all nodes, if we take a functional identity initial distribution $P(\nu) = \mathbb{I}(\nu - \nu_F)$, where ν_F is some initial message, the population dynamics algorithm is not necessary: we only have to consider the updating of ν_F.

In the next sections we show the results obtained in Bethe and ER graphs for different p and c values. The results presented were obtained with population sizes up to $N = 6 \times 10^5$.

IV. *XY* AND *p*-CLOCK MODELS ON RANDOM REGULAR GRAPHS

In this section we show the results obtained for the FM ($J = 1$) 4-XY model on Bethe lattices: the degree of variable nodes is fixed to c, while that of function nodes is $k = 4$. In order to numerically find the equilibrium distributions solving Eqs. (19) and (20) for the XY model, we resort to the discrete p-clock model [cf. Eq. (8)]. Writing $\nu_a \equiv \nu(\phi_a)$, at fixed c Eqs. (19) and (20) become

$$\hat{\nu}_a \stackrel{d}{=} \frac{1}{z_{\text{test}}} \prod_{l=1}^{3} \left(\sum_{a_l=0}^{p-1} (\nu^l)_{a_l} \right) e^{\beta J \cos\frac{2\pi}{p}(a_1 - a_2 + a_3 - a)}, \quad (23)$$

$$\nu_a \stackrel{d}{=} \frac{1}{z_{\text{cav}}} \prod_{m=1}^{c-1} (\hat{\nu}^m)_a. \quad (24)$$

In order to study possible fixed-point solutions of Eqs. (23) and (24), it is useful to introduce the discrete Fourier transform (DFT) of the message ν,

$$c_k = \sum_{a=0}^{p-1} \nu_a e^{\frac{-2\pi i k a}{p}}, \quad (25)$$

whose inverse transform is

$$\nu_a = \frac{1}{p} \sum_{k=0}^{p-1} c_k e^{\frac{2\pi i k a}{p}}. \quad (26)$$

From Eq. (25) we note that ν_a is real; that is,

$$\sum_{k=0}^{p-1} c_k e^{\frac{2\pi i k a}{p}} = \left(\sum_{k=0}^{p-1} c_k e^{\frac{2\pi i k a}{p}} \right)^* = \sum_{k=0}^{p-1} c_k^* e^{\frac{2\pi i (p-k) a}{p}}$$

and $c_k = c_{p-k}^*$. In particular, $c_{p/2}$ is real. Furthermore, $c_0 = p/(2\pi)$ and Eq. (26) can be rewritten as

$$\nu_a = \frac{1}{2\pi} \left(1 + \sum_{k=1}^{p-1} \frac{2\pi}{p} c_k e^{\frac{2\pi i k a}{p}} \right). \quad (27)$$

Expressing the discrete Fourier transform of the cavity function in terms of the magnitude and phase, $c_k \equiv |c_k| e^{i\theta_k}$,

Eqs. (23) and (24) become

$$\hat{\nu}_a \stackrel{d}{=} \frac{1}{2\pi} + \frac{1}{2\pi p^3 I_0^p(\beta J)} \times \left[I_{p/2}^p(\beta J) \prod_{l=1}^{3} \left(c_{p/2}^{(l)}\right)(2\pi)^3(-1)^a + \sum_{k=1}^{p/2-1} I_k^p(\beta J) \left(\prod_{l=1}^{k-1} |c_k^{(l)}| \right) (2\pi)^3 \times 2\cos\left(\theta_k^{(1)} - \theta_k^{(2)} + \theta_k^{(3)} + \frac{2\pi a k}{p}\right)\right], \quad (28)$$

where I_k^p indicates the discrete approximation of the modified Bessel function of the first kind,

$$I_k^p(w) = \frac{1}{p} \sum_{a=0}^{p-1} e^{w\cos(\frac{2\pi a}{p})} \cos\left(k\frac{2\pi a}{p}\right), \quad (29)$$

that, for $p \to \infty$, tends to the well-known

$$I_k(w) = \frac{1}{2\pi} \int_0^{2\pi} e^{w\cos\phi} \cos(k\phi)\,.$$

Equation (28) is a distributional equality where $c^{(1)}$, $c^{(2)}$, and $c^{(3)}$ indicate the discrete Fourier transform of three i.i.d. ν's. It can be observed that the trivial population distribution is $P(\nu) = \mathbb{I}(\nu - \nu_{\rm PM})$, where $(\nu_{\rm PM})_a = 1/(2\pi)\ \forall\, a$, i.e.; when all $c_k^{(l)} = 0$, this is a fixed-point solution of Eqs. (23) and (24) for all values of βJ. It is referred to as the paramagnetic (PM) solution, invariant under Z_p symmetry, which is a discretization of the SO(2) symmetry: there are no preferred directions in the system and the spins are uniformly randomly oriented. We can note that, as $p \to \infty$, we obtain the correct, SO(2)-invariant limit for the XY PM solution [cf. Eqs. (23) and (24)].

The fact that the uniform distribution is always a solution does not necessarily mean that the thermodynamic phase is always the PM one. In given regions of the phase diagram, Eqs. (23) and (24) admit more than one fixed-point solution and the behavior of the model can be correctly described by a non-PM solution. It is important to note that any other solution for which at least one of the c_k is different from 0 is not invariant under Z_p. Therefore, if the system admits solutions other than the PM one, there will be spontaneous symmetry breaking.

In the case of an FM solution, the system can align itself among p possible degenerate solutions, whose phases are linked by the transformations of Z_p. Once the populations $P(\nu)$ and $Q(\hat{\nu})$ are computed, we can evaluate the distribution of the marginal probabilities of variable nodes,

$$\mu(\phi) \stackrel{d}{=} \frac{1}{z_s} \prod_{l=1}^{c} [\hat{\nu}^l(\phi)], \quad z_s = \int_0^{2\pi} d\phi \prod_{m=1}^{c} [\hat{\nu}^m(\phi)], \quad (30)$$

and, consequently, the magnetization, m_x and m_y, and the free energy, $f(\beta)$. In the continuous $p \to \infty$ limit we have, for the magnetization,

$$\langle m_x \rangle = \mathbb{E}_{\{\mu\}}\left(\int_0^{2\pi} d\phi \mu(\phi) \cos\phi \right),$$
$$\langle m_y \rangle = \mathbb{E}_{\{\mu\}}\left(\int_0^{2\pi} d\phi \mu(\phi) \sin\phi \right) \quad (31)$$

and, for the free energy,

$$-\beta f(\beta) = \mathbb{E}_{\{\hat{\nu}\}} \log z_s + \frac{c}{K} \mathbb{E}_{\{\nu\}} \log z_c - c\mathbb{E}_{\{\nu,\hat{\nu}\}} \log z_l, \quad (32)$$

where

$$z_c = \int_0^{2\pi} \left[\prod_{j=1}^{4} d\phi_j \nu^j(\phi_j) \right] e^{\beta J \cos(\phi_1 - \phi_2 + \phi_3 - \phi_4)},$$
$$z_l = \int_0^{2\pi} d\phi \nu(\phi)\hat{\nu}(\phi),$$
$$z_s = \int_0^{2\pi} d\phi \left[\prod_{m=1}^{c} \hat{\nu}^m(\phi) \right].$$

For the p-clock free energy Eq. (32) becomes

$$-\beta f(\beta) = \log\frac{2\pi}{p} + \mathbb{E}_{\{\hat{\nu}\}} \log \sum_{a=0}^{p-1} \prod_{m=1}^{c} \left(\hat{\nu}_a^m\right) - c\mathbb{E}_{\{\nu,\hat{\nu}\}} \log \sum_{a=0}^{p-1} \nu_a \hat{\nu}_a + \frac{c}{k} \mathbb{E}_{\{\nu\}} \log \prod_{j=1}^{k} \sum_{a_j=0}^{p-1} \nu_{a_j} \times e^{\beta J \cos\frac{2\pi}{p}(a_1 - a_2 + a_3 - a_4)}. \quad (33)$$

In the PM solution ($m_x = m_y = 0$) the free energy of the p-clock model is

$$f^p(\beta) = -\frac{1}{\beta}\left(\log 2\pi + \frac{c}{k} \log I_0^p(\beta J) \right), \quad (34)$$

where $I_0^p(w)$ is defined in Eq. (29). When a solution other than the PM one appears, we may have m_x or m_y or both different from 0: the total magnetization displays a preferred direction and we have an FM solution. The symmetry Z_p is restored if we note that all the p states can appear with the same probability $1/p$ and we take the average over *pure states*:

$$m_{x,y} = \sum_{a=0}^{p-1} \frac{1}{p} m_{x,y}^a,$$

where $m_{x,y}^a$ are the magnetization values in state a.

Eventually, the system at low temperatures can also be found in a *phase-locked* (PL) phase, where $m_{x,y} = 0$ but phases are nevertheless locked into a nontrivial relation among them. Since Eq. (31) is 0, because

$$\int d\phi \mu(\phi) \cos\phi = \int d\phi \mu(\phi) \sin\phi = 0, \quad \forall \mu(\phi)\,,$$

the order parameter to spot such a PL phase is

$$r = 2\mathbb{E}_{\{\mu\}} \int d\phi \mu(\phi) \cos^2\phi - 1. \quad (35)$$

This is trivially equally to 0 in the PM phase but it acquires a different value, $r \in [-1, 1]$, when the system is in the PL phase.

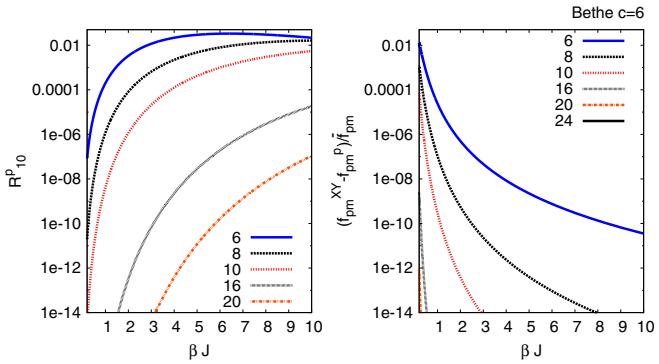

FIG. 1. (Color online) Left: R^p_{01} as a function of βJ for $c = 6$. We can see that as p increases the convergence to the XY model holds up to larger and larger β values. For $p = 20 (p + 2 = 22)$, the difference between the two is smaller than double precision up to values of $\beta J \simeq 3$. Right: Convergence of the p-clock paramagnetic free energy to the XY paramagnetic free energy for $c = 6$. The denominator is $\bar{f}_{\rm pm}(\beta) \equiv (f^p_{\rm pm} + f^{XY}_{\rm pm})/2$. The relative difference between the two decreases with βJ.

A. p-clock convergence to XY

Considering Eq. (28) we derive the main features of the solutions as a function of the number of clock states p. We can, thus, check what is the minimum number of values of the XY angles to obtain an effective description of the model with continuous XY spins. The 4-XY PM/FM phase transition, unlike the case with only two-body interaction terms ($k = 2$) [28], turns out to be first-order, discontinuous in internal energy and in order parameters. In general, the number p guaranteeing convergence between p-clock and XY models will depend on the temperature range. In particular, we compare (i) spinodal points, (ii) PM free energies, and (iii) FM free energies to establish convergence of the two models. (i) Indicating as β_s the inverse temperature of the FM spinodal, as p increases,

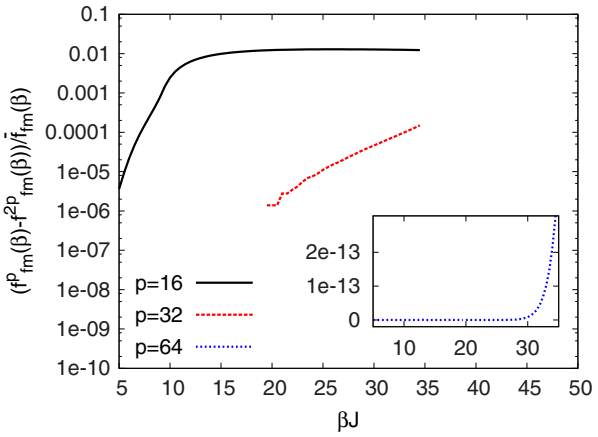

FIG. 2. (Color online) Relative free energy difference of the FM phase for different $p, 2p$ couples of p-clock models. The denominator is $\bar{f}_{\rm fm}(\beta) \equiv (f^{(p)}_{\rm fm} + f^{(2p)}_{\rm fm})/2$. Already for $p = 16$ and $p = 32$ the relative difference saturates at 10^{-2} for $\beta J > 10$. Inset: Practically no difference can be appreciated in double precision between $p = 64$ and $p = 128$ up to $\beta J \simeq 30$.

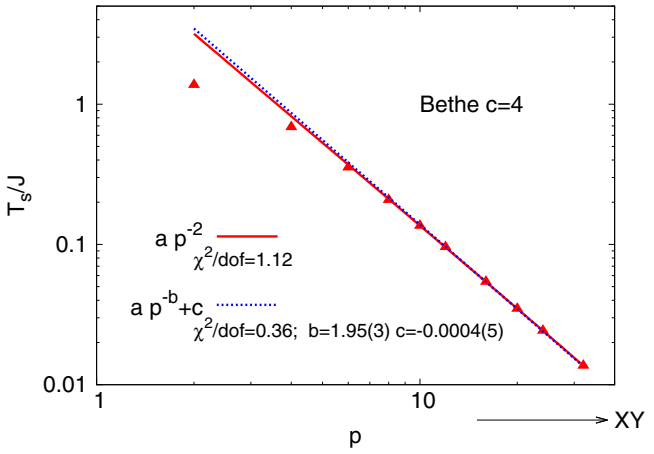

FIG. 3. (Color online) Spinodal temperature, T_s, as a function of p, with its best fits for vanishing T_s in the $p \to \infty$ limit for fixed connectivity $c = 4$. For continuous XY spins, when $T > 0$, the only fixed-point solution of BP equations is the paramagnetic solution. The fact that we obtain a ferromagnetic solution is an artifact induced by $p < \infty$.

$\beta_s^{p+2} \geqslant \beta_s^p$ holds. This derives from the fact that [cf. Eq. (29)]

$$R^p_{01}(x) \equiv \frac{I^p_1(x)}{I^p_0(x)} - \frac{I^{p+2}_1(x)}{I^{p+2}_0(x)} \geqslant 0. \tag{36}$$

The behavior of Eq. (36) is plotted in the left panel in Fig. 1. (ii) The PM free energy can be computed analytically, for both the p-clock and the continuous XY model. We can, therefore, evaluate the number of spin states, p, needed to converge to the XY model in the desired temperature interval also from the PM free energy difference (cf. the right panel in Fig. 1). (iii) In Fig. 2 a numerical comparison of the FM free energy is shown between p-clock models with, respectively, p and $2p$ states. As becomes clear in the inset, already for $p = 64$ no difference can be further appreciated for very high β values, much larger than the critical β_c, as will soon be shown. We also stress that at very low temperatures a direct comparison with the XY-model free energy cannot be performed, because the latter continuous model has an ill-defined entropy at $T = 0$ and its free energy is, thus, defined except for a constant. Comparison with the XY model, thus, implies the necessity of introducing a (p-dependent) constant.

In Figs. 3 and 4 we report the results obtained for the spinodal and critical point as a function of the number of states p for different values of the connectivity, $c = 4,5,6$. At the critical inverse temperature $\beta_c = 1/T_c$ the PM solution becomes metastable. As we can see in Fig. 3, the lower critical connectivity for the XY model is $c_{\rm low} = 5$: FM solutions for $c = 4$ are an artifact of taking ϕ as a discrete variable. In Fig. 4 we show the convergence to the XY limit in p for $c = 5,6$. The convergence is faster for the spinodal point but not much slower for the critical point. This result is expected from the properties of the Bessel functions we outlined in Fig. 1: seeing that $T_c < T_s$, the number of p needed to achieve convergence to the XY limit is larger. From these results we can conclude that the $p \simeq 20$-clock spin is already a rather good approximation of the planar continuous spin for what is concerned in the analysis of the critical behavior.

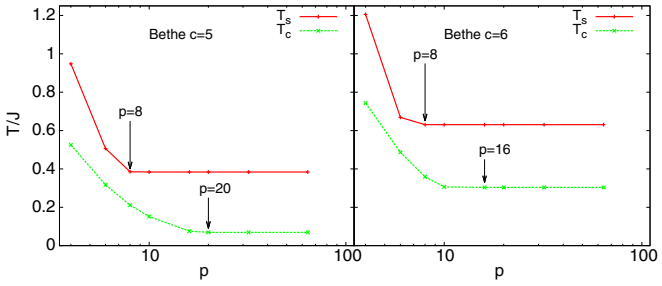

FIG. 4. (Color online) Spinodal and critical temperatures T_s and T_c vs p in the Bethe lattice, for $c = 5$ (left) and $c = 6$ (right): the values of p for which convergence to the XY limit is attained are indicated by arrows.

B. Critical behavior of the 4-XY model

We thus study the properties of the XY model across the critical point using a $p = 64$-clock model. In Fig. 5 we display the free energy for $c = 6$ as a function of βJ for the three fixed-point solutions of BP equations, (27) and (28): the PM, FM, and PL phases. The FM solution is selected by tuning the initial conditions, assigning a higher probability to a given ϕ value. The PL solution is obtained at high enough β when initial $\nu(\phi)$ are given with two peaks at opposite angles. In Fig. 6 we report the resulting marginal cavity distributions for the phase values, $\nu(\phi)$ and $\hat{\nu}(\phi)$.

In the PL phase, though at each local instance $m_{xy} = 0$, the parameter r defined in Eq. (35) is not. Its free energy behavior is shown in Fig. 5 as the dashed line. It can be observed that the PL phase is always metastable with respect to the FM phase, though, for higher β its free energy becomes lower than the PM free energy. Because of the observed numerical fragility of this solution with respect to the PM and the FM phases, it is hard to discriminate its spinodal point. With the computation performed so far the PL phase appears to occur at $\beta J \gtrsim 4.5$.

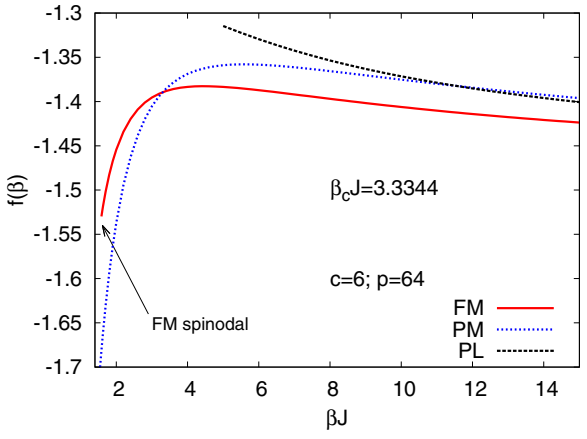

FIG. 5. (Color online) Free energy, $f(\beta)$, vs βJ for $c = 6$ and $p = 64$. The solid line refers to the ferromagnetic fixed-point solution found considering as initial conditions the effect of a strong external magnetic field. The dotted line refers to the paramagnetic solution. Unlike in the $k = 2$ case, the paramagnetic solution is stable at every temperature. The dashed line represents the metastable phase-locked solution.

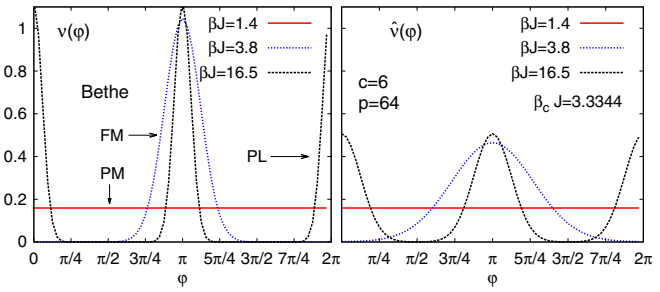

FIG. 6. (Color online) ν_a and $\hat{\nu}_a$ for $p = 64$ and three phases at three values of βJ: PM at $\beta J = 1.4 < \beta_c J$, FM at $\beta J = 3.8 > \beta_c J$, and PL at $\beta J = 16.5$.

V. XY AND p-CLOCK MODELS ON ERDÒS-RÉNYI FACTOR GRAPHS

If the degrees of variable nodes are i.i.d. random variables, the local environment is not the same everywhere in the graph. In the ER case BP equations are *distributional equations* as in Eqs. (23) and (24), where the number of neighbors to a variable node is extracted by means of a Poissonian distribution of average c.

In this section we show the results obtained by applying the population dynamics algorithm to the ordered p-clock model on ER graphs and look for asymptotic solutions as $p \to \infty$. The results presented were obtained with a population size up to $N = 6 \times 10^5$. The code used to numerically determine $\nu, \hat{\nu}$ stationary populations for large p is a parallel code running on GPUs. This sensitively speeds up the population update of $\hat{\nu}$ (requiring Np^k operations) with respect to a serial, CPU-running code.

In Fig. 7 we show the values obtained for T_s/J when the mean connectivity of variable nodes is $\langle c \rangle = 5$. We can see that in this case the only solution in the $p \to \infty$ limit is the PM solution, whereas other solutions with $\langle m^2 \rangle \neq 0$ are artifacts of $p < \infty$.

In Fig. 8 we report the results obtained when $\langle c \rangle = 6$ and 8: as for regular random graphs the convergence to the XY

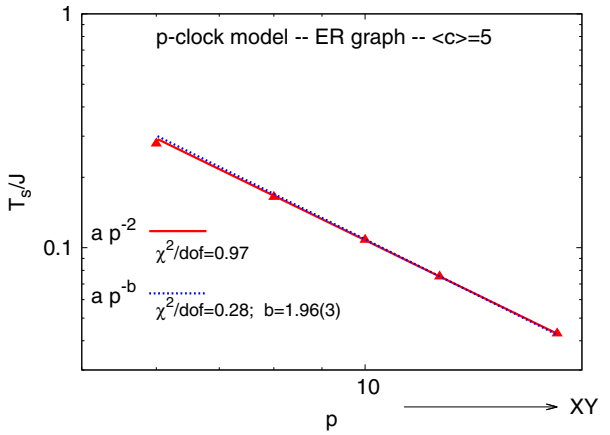

FIG. 7. (Color online) Spinodal point values T_s/J vs p on Erdòs-Rényi factor graphs with mean connectivity $\langle c \rangle = 5$. Interpolations displayed are both consistent with the absence of a magnetized phase in the XY, for $T > 0$.

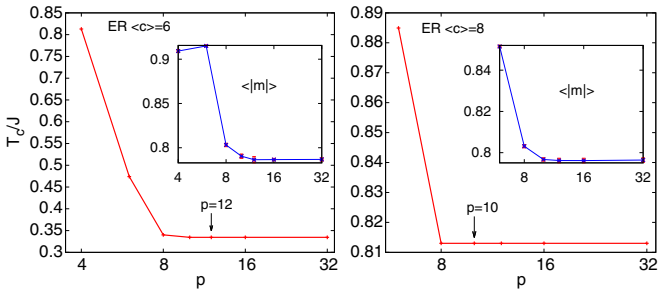

FIG. 8. (Color online) Critical point as a function of integer p on Erdòs-Rényi factor graphs with mean connectivity $\langle c\rangle = 6$ (left) and $\langle c\rangle = 8$ (right). Insets: Absolute values of the magnetization as a function of p.

model is rather fast (see also the inset for the absolute value of the magnetization). We observe that $c_{\rm low} = 6$ for the ER graph is larger than the corresponding value, $c_{\rm low} = 5$, in the Bethe lattice. When $\langle c\rangle = 5$, with an ER distribution, the probability of having a connectivity of less than 5 is $P(c < 5) \sim 0.44$: the presence of many nodes with connectivity 4 or lower apparently leads to a zero transition temperature in the ER graph. We note, however, that in the linear case ($k = 2$) the trend is the opposite: for Bethe lattices the minimal connectivity for a nontrivial critical behavior is $c_{\rm low} = 3$, and for ER graphs it is $c_{\rm low} = 2$, as reported in the Appendix, where we derive the analytic linear expression for T_c vs $1/c$.

VI. MODE-LOCKING ON RANDOM GRAPHS

As mentioned in Sec. I, the nonlinear XY model can be used to describe the phase dynamics of interacting electromagnetic modes in lasers. Previous mean-field studies on fully connected models assume *a narrow band* for the spectrum [8,12–14]; that is, all modes have practically the same frequency, and in this way, the frequencies do not play any role in the system behavior. This is the case for the systems analyzed in Secs. IV and V. In this section, exploiting the diluted nature of the graphs, we deepen this description and allow for the existence of finite-band spectra and gain frequency profiles.

Tree-like factor graphs can be built where each variable node, representing a light mode, has a quenched frequency associated with its dynamic phase. The frequencies are distributed among modes according to, e.g., a Gaussian or a parabolic distribution proportional to the *optical gain* $g(\omega)$ for the system resonances. The graph is, then, constructed starting from the root in such a way that the FMC, Eq. (1), is satisfied for each interacting quadruplet. In other words, a function node m *is* an FMC for the $\{\partial m\}$ modes connected to it. As an example, in Fig. 9, we show a possible frequency distribution for a tree-like factor graph in which the connectivity of the variable nodes is fixed at $c = 6$. The open (large) triangles refer to the gain profile, $g_{\rm in}(\omega)$, according to which the frequencies are assigned to free variable nodes (two-thirds of the total). The remaining one-third of the node frequencies are assigned according to the FMC. Note that, applying the FMC, one can obtain three possible independent combinations for the fourth frequency. In Fig. 9 we see that the frequency distribution of all frequencies, $g(\omega)$, evaluated once the FMC has been imposed

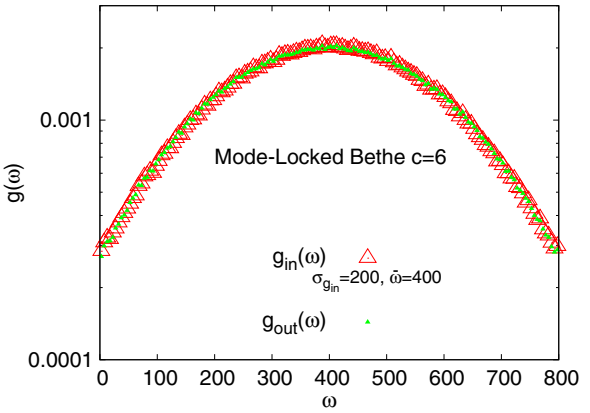

FIG. 9. (Color online) Open triangles refer to the distribution of frequencies assigned to two-thirds of the variable nodes, according to a Gaussian gain profile, $g_{\rm in}(\omega)$, of mean $\bar\omega = 400$ and variance $\sigma_{g_{\rm in}} = 200$. Filled triangles represent to the distribution $g_{\rm out}(\omega)$ we obtain once the FMC is imposed: $g_{\rm out}(\omega)$ coincides with $g_{\rm in}(\omega)$ on the whole domain.

for all quadruplets, is compatible with the starting one, $g_{\rm in}(\omega)$. This result shows that, considering a generic Gaussian gain profile, sparse factor graphs, in which $\langle c\rangle = \mathcal{O}(1)$, can yield a meaningful realistic description of nonlinearly interacting modes whose frequencies satisfy the FMC.

A. Phases and phase-locking

Once graphs with fixed connectivity and frequency matching function nodes are introduced we can study the critical behavior considering βJ as the pumping rate squared $\mathcal{P}^2$ [cf. Eq. (6)] in the context of lasing systems. We term these graphs "mode-locking Bethe" (ML-Bethe) lattices. As a result of BP, above a certain threshold of $\mathcal{P}$ mode phases turn out to show a peculiar behavior of the frequencies: $\phi(\omega)$ coincides with the linear law of Eq. (2), as shown in Fig. 10 for different

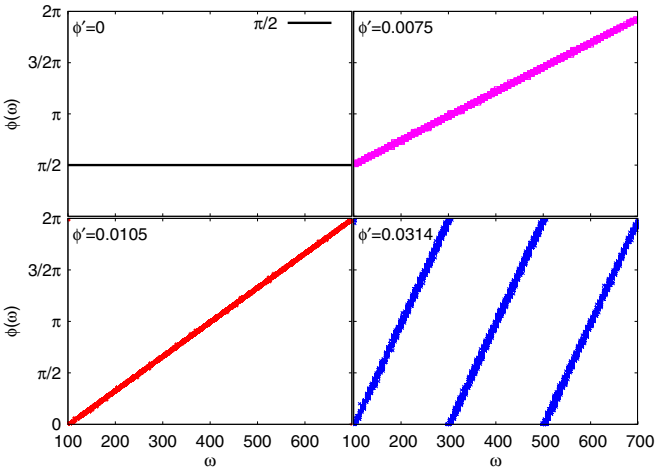

FIG. 10. (Color online) Phases vs frequencies in phase-locked phases on an ML-Bethe lattice with $c = 6$, $N_{\rm shell} = 5$, and the total number of inner nodes (excluding leaves) $N_{\rm bulk} = 4339$. The number of clock tics is $p = 120$. The number of frequencies is $N_\omega = 88$ or 120. The pumping rate squared is $\mathcal{P}^2 = \beta J = 7$.

linear coefficients ϕ'. Though, generically, the magnetizations are $m_{xy} = 0$, the phases are, nevertheless, found to be locked. This is the typical behavior established at the lasing threshold by nonlinearity in multimode lasers. In the above-mentioned construction of the ML-Bethe lattice, frequencies are assigned to modes with a probability proportional to the gain profile.

We take into account two qualitatively different cases. First, we consider the case where only equispaced frequencies are eligible: this is a proxy for the so-called *comb* distribution [29,30], in which many resonances occurs with a linewidth much smaller than the fixed resonance interspacing. Furthermore, we investigate the opposite extreme, the *continuous* case, in which each mode frequency is extracted continuously from the whole gain band with no further constraint on their values, other than FMC.

In Fig. 10 we show different realizations of such phase-locking, all of them with different *phase delay* ϕ'. They are frequency independent and do not depend on the frequencies being equispaced or continuously distributed. This amounts to saying that the phase delay dispersion is 0. Each locking is obtained by means of different boundary conditions at the external shell. The case $\phi' = 0$ is also achieved, which is the FM phase: all modes are locked at the same phase. In term of thermodynamics all realizations of phase-locking, including the FM one, display comparable free energies, all of them definitely different from the free energy of the coexisting PM phase.

Altough phase-locking [cf. Eq. (2)] occurs in both the comb and the continuous frequency distributions, as shown in Fig. 11 there is a difference in the range of values that frequencies can take at each (discrete) value of the phases. We anticipate that only in the case of comb-like distributions of gain resonances will mode-locking allow the realization of *ultrashort pulses*.

We, eventually, come to the analysis of the electromagnetic signal for a wave system with $N = N_{\text{bulk}}$ modes and N_ω

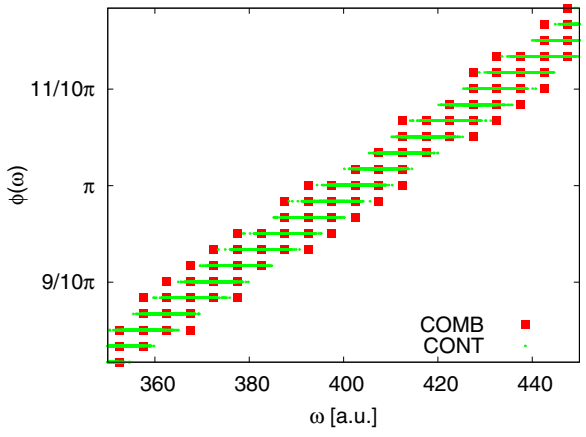

FIG. 11. (Color online) Detail of the behavior of the phases vs frequencies extracted by means of the distribution in Fig. 9, both as continuous and as comb-like, equispaced at $\beta J = 7$, for $c = 6$, $N_{\text{shell}} = 4339$, $N_{\text{bulk}} = 65\,089$, and $p = 120$, for 120 continuous [light-gray (green) points] and comb [dark-gray (red) squares] frequencies.

frequencies,

$$E(t) = \sum_{k=1}^{N} A_k e^{\imath(\omega_k t+\phi_k)} = e^{\imath(\omega_0 t+\phi_0)} \sum_{k=1}^{N} A_k e^{\imath(\Delta\omega_k t+\Delta\phi_k)}, \tag{37}$$

where the sinusoidal carrier wave frequency ω_0 is the central frequency of the spectrum (of the order of 10^{15} rad $\cdot$ s^{-1}), $\Delta\omega_k$'s are of the order of radio frequencies (ca. 10^9 rad $\cdot$ s^{-1}), and $\phi_0 = \phi(\omega_0)$ is the phase of the mode at the central frequency. In the ML regime, where [cf. Eq. (2)] $\Delta\phi_k = \phi'\Delta\omega_k$, the time-dependent overall amplitude can be written as

$$A(t) \equiv \sum_{k=1}^{N} A_k e^{\imath(\Delta\omega_k t+\Delta\phi_k)} = \sum_{k=1}^{N} A_k e^{\imath\Delta\omega_k(t+\phi')} = A(t+\phi'). \tag{38}$$

The term phase (or group) delay for ϕ' comes from the fact that it corresponds to a shift in time in the $E(t)$ carrier peak with respect to the $|E(t+\phi')| = |A(t+\phi')|$ *envelope* maximum. If, furthermore, N_ω comb-distributed resonances are considered with interspacing $\Delta\omega$, we can write

$$e^{\imath\Delta\omega_k t} = n_l e^{\imath l\Delta\omega t}, \quad k = 1,\ldots,N, \quad l = -N_\omega/2,\ldots,N_\omega/2-1, \tag{39}$$

where n_l is the number of modes at frequency $l\Delta\omega$. This is the case for ultrashort ML lasers for which very short and very intense periodic pulses occur, as shown for $N_{\text{bulk}} = 4339$ modes in the first and third left-hand panels in Fig. 12 for $\phi' = 0.0314$ ($N_\omega = 120$) and $\phi' = 0.0075$ ($N_\omega = 88$), respectively.

Since we are working in the quenched amplitude approximation with intensity equipartition, each mode has magnitude $A_k = 1$. However, we are using diluted interaction networks, and consequently, the same frequency can be taken by modes localized in different spatial regions, whose number we denote n_l in Eq. (39). Therefore,

$$E(t) = e^{\imath(\omega_0 t+\phi_0)} \sum_{l=-N_\omega/2}^{N_\omega/2-1} n_l e^{\imath l\Delta\omega(\phi'+t)}, \tag{40}$$

and from the point of view of the Fourier decomposition of the electromagnetic signal, n_l plays the role of the amplitude of the modes at frequency l.

A detail of the pulses is shown in the first and third right-hand panels in Fig. 12. The linear behaviors shown in Fig. 10, like Eq. (2), imply that the signal is *unchirped*. In other words, the phase delay displays no dispersion and the frequency of oscillation of the carrier remains the same for all pulses, as shown in the right-hand panels in Fig. 12. The period of the pulses is $\tau_p = 2\pi/\Delta\omega$, where $\Delta\omega = 5$ for phase delay $\phi' = 0.0314$ and $\Delta\omega = 7$ for $\phi' = 0.0075$. The pulse duration is expressed in terms of its full width at half-maximum $\Delta\tau_p$, also compatible with the time it takes for the electromagnetic field amplitude, $A(t)$, to decrease below the noise level from its maximum.

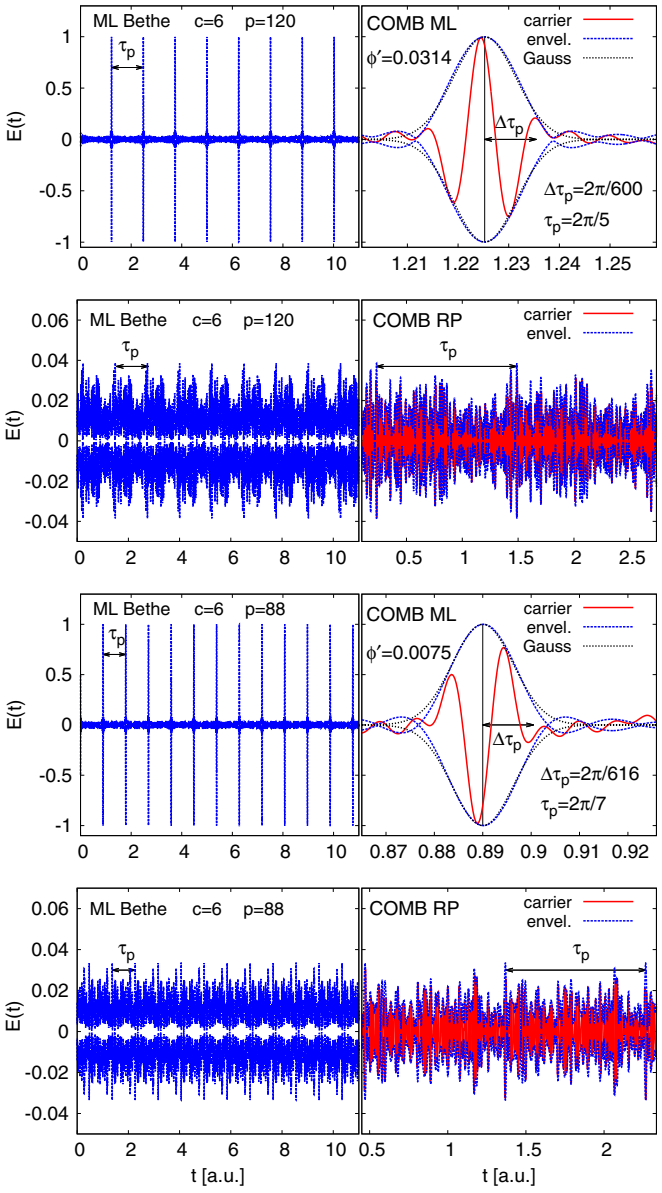

FIG. 12. (Color online) The laser pulse $E(t)$ generated in the lasing phase in an ML-Bethe lattice with a comb-like frequency distribution. Two realizations of the phase-locking are reported, with delay $\phi' = 0.0314$ (top four panels) and $\phi' = 0.0075$ (bottom four panels). In the left panels several periodic pulses are shown, with period $\tau_p = 2\pi/\Delta\omega$ and with $\Delta\omega = 5$ in the top case and $\Delta\omega = 7$ in the bottom case. In the right panels details of the single pulse are given, where both carrier and envelope are plotted. In the ML pulsed phase (first and third right-hand panels) the pulse full width half maximum is $\Delta\tau_p = 2\pi/(N\Delta\omega)$, where $N = 120$ for $\phi' = 0.0314$ and $N = 88$ for $\phi' = 0.0075$. We also plot the behavior of the amplitude $\pm|E(t)|$ expected for Gaussian gain profiles, i.e., the square root of (41), which displays a rather good coincidence.

In ML ultrafast lasers, if the gain has a Gaussian profile at equidistant frequencies, and consequently, n_l is so distributed [cf. Eq. (40)], the signal amplitude squared is expected to behave like

$$|E(t)|^2 = |E(t_{\max})|^2 \exp\left\{-\left(2\frac{t - t_{\max}}{\Delta\tau_p}\right)^2 \ln 2\right\} \qquad (41)$$

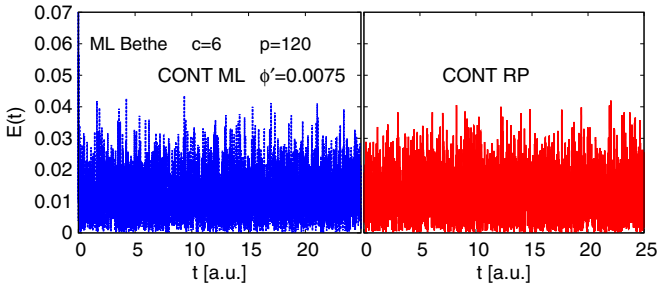

FIG. 13. (Color online) The amplitude of the e.m. field, $|E(t)|$ [cf. Eq. (38)], is plotted for an ML-Bethe lattice with a continuous frequency distribution. We display the $\phi' = 0.0075$ case in the high-pumping mode-locked regime (left) and in the low-pumping random phase regime (right). This scenario is independent of the value of ϕ'.

in the limit of very many frequencies ($\Delta\omega \to 0$) [31]. In Fig. 12, first and third right-hand panels, this behavior is labeled "Gauss." Above the noise level it appears to coincide very well with the envelope obtained by Fourier transform of the output of BP equations on ML-Bethe lattices.

In the second ($\phi' = 0.0314$) and fourth ($\phi' = 0.0075$) rows in Fig. 12 we show $E(t)$ in the low-pumping PM phases, where modes display random phases (RP). The periodicity induced by the comb-like distribution appears also here, though the electromagnetic field is purely noisy, without any pulse.

When frequencies are taken in a continuous way the coherent PL phase turns out to display a much less intense coherent signal, with no pulses, as shown in Fig. 13, where $|E(t)|$ is shown both in the ML and in the random phase (PM) regimes, with no apparent difference in the time domain between coherent and incoherent light.

VII. CONCLUSIONS

In the present work we have investigated the XY model with nonlinear, four-body interaction and its discrete approximant, the so-called p-clock model, on random graphs. Cavity equations have been derived and solved for the Bethe lattice and the ER graph, carrying out a thorough analysis of the critical behavior of temperature at varying connectivity values. Three phases are found for these models. At high T the systems are in a PM phase. At low T the dominat thermodynamic phase is FM; that is, an SU(2) continuous symmetry breaking occurs in the XY model and a Z_p discrete symmetry breaking occurs in the p-clock model. Otherwise, a low-temperature metastable *phase-locking* phase can be reached, in which the magnetization is 0 but the phases, though all different, are nevertheless correlated with each other. An accurate study of the convergence of the p-clock model to the continous model is performed and presented.

The models introduced can be applied to laser optics, where XY or p-clock spins play the role of light mode phases. In this photonic framework the inverse temperature β is proportional to the square of the rate of population inversion, the so-called pumping rate, driving the lasing transition from the incoherent light regime. The first result is that a mode-locking Bethe lattice can be consistently built in, where, besides the phase, also a frequency is associated with each variable node and

each function node acts as an FMC among four frequencies [cf. Eq. (1)]. The latter is a common kind of nonlinear interaction occurring in standard ultrafast multimode lasers. As β increases the system is found to undergo a mode-locking transition: phases at nearby frequencies are locked to take a fixed amount, and a linear $\phi(\omega)$ relationship like Eq. (2) is established at the critical point. In the case of evenly distributed mode frequencies this leads to a pulsed laser, i.e., a laser whose electromagnetic field oscillations are characterized by a train of very short and very intense pulses. We have compared the results obtained in this case to the laser signal for multimode frequencies randomly taken in a continuous dominion, as well as to the incoherent signal below the lasing threshold. The model presented, thus, provides an analytical and phenomenologically accurate description of multimode lasers at the level of the *single* pulse, which can be chosen arbitrarily shorter than the period between two pulses when the frequencies are evenly spaced as, e.g., in standard Fabry-Perot cavities. Such a limit is not achievable experimentally because the typical response time of conventional photodetectors is of the order of 1 ns, whereas the duration of pulses in ultrafast mode-locking solid-state or semiconductor lasers ranges from the order of a picosecond to the order of a femtosecond.

Eventually, laser emission is also investigated in the opposite extreme, where frequencies can take any value according to a given gain profile, not just evenly spaced values. These systems undergo phase-locking, because of the FMC, but prove a far less intense signal, more akin to the signal of early continuous-wave pumped solid-state lasers [32]. Such a frequency limit distribution is, in principle, compatible with the random topology of light localizations on sparsely connected interaction networks, which can represent a salient feature of more complex laser systems called random lasers [16,33–36]. In these systems, indeed, where also the magnitude and even the sign of the mode-coupling can be disordered, the pumping rate threshold values are known to be higher and the signal intensity is found to be sensitively smaller than in standard *ordered* multimode lasers.

ACKNOWLEDGMENTS

The research leading to these results received funding from the Italian Ministry of Education, University and Research under the Basic Research Investigation Fund (FIRB/2008) program/CINECA Grant No. RBFR08M3P4 and under the PRIN2010 program, Grant No. 2010HXAW77-008, and from the People Programme (Marie Curie Actions) of the European Union's Seventh Framework Programme FP7/2007-2013 under REA Grant Agreement No. 290038, NETADIS project.

APPENDIX: XY MODE WITH LINEAR INTERACTION ON SPARSE GRAPHS

Let us consider the two-point correlation function for the XY model with pairwise interaction, $k = 2$:

$$\mathcal{H} = -\sum_{(i,j)} J_{ij} \cos(\phi_i - \phi_j). \tag{A1}$$

Taking two variable nodes, i and j, we indicate by U_{ij} the shortest path that goes from i to j; by F_R, the subset of function nodes (now simple links) in U_{ij}; and by V_R, the subset of variable nodes in U_{ij} including i and j. Then let ∂R be the subset of function nodes that are not in U_{ij} but are adjacent to the variable nodes in V_R: $\forall m \in \partial R, \exists' l \in \partial m \bigcap V_R$, which is called $l(m)$. Then we have that the joint probability distribution of all variables in R is

$$\mu(\underline{\phi_R}) = \frac{1}{Z_R} \prod_{m \in F_R} \psi_m(\phi_{\partial m}) \prod_{m \in \partial R} \hat{\nu}_{m \to l(m)}(\phi_{l(m)}). \tag{A2}$$

We then denote by r the distance between the two initial spins, i and j. The distance r is, in fact, the number of links in F_R, each one with its marginal $\hat{\nu}$. Recalling Eq. (11) we obtain that, in the PM phase [where $\hat{\nu}(\phi) = \frac{1}{2\pi}$, $\forall \phi \in [0,2\pi)$], the two-spin joint probability distribution function is

$$\mu(\phi_i,\phi_j) = \frac{1}{(2\pi)^2} + \frac{1}{(\pi I_0(\beta J))^r} \times \sum_{n=1}^{\infty} (I_n(\beta J))^r \cos(n(\phi_i - \phi_j)). \tag{A3}$$

Consequently,

$$\langle \cos(\phi_i)\cos(\phi_j)\rangle = \langle \sin(\phi_i)\sin(\phi_j)\rangle = \frac{1}{2}\left(\frac{I_1(\beta J)}{I_0 \beta J}\right)^r$$

and

$$C(r) \equiv \langle \cos(\phi_i - \phi_{i+r})\rangle = \left(\frac{I_1(\beta J)}{I_0(\beta J)}\right)^r. \tag{A4}$$

The susceptibility can be written as

$$\chi = \frac{1}{N}\sum_{r=0}^{\infty} \sum_{(i,j=i+r)\in\mathcal{G}} \langle \sigma_i \sigma_j \rangle = \sum_{r=0}^{\infty} \mathcal{N}(r) \left(\frac{I_1(\beta J)}{I_0(\beta J)}\right)^r, \tag{A5}$$

where $(i,i+r)$ indicates all the links in the graph between two variable nodes at distance r and $\mathcal{N}(r)$ is the expected number of variables nodes j at a distance r from a uniformly random node i. For large r on a Bethe graph with fixed connectivity c, $\mathcal{N}(r) = (c-1)^r$ and $\chi < \infty$ for

$$\left(\frac{I_1(\beta J)}{I_0(\beta J)}\right)(c-1) < 1. \tag{A6}$$

As

$$\left(\frac{I_1(\beta_c J)}{I_0(\beta_c J)}\right)(c-1) = 1, \tag{A7}$$

$\chi = \infty$, the PM solution becomes unstable and the value of the critical temperature $T_c = \frac{1}{\beta_c}$ is determined.

For the case of ER graphs, we obtain, for large r, $\mathcal{N}(r) = \langle c \rangle^r = c^r$, where we have used the result of the Poissonian distribution $P_c(k)$, where k indicates the random connectivity of a uniform variable node:

$$\sum_{k=2}^{\infty}(k-1)P_c(k-1) = \sum_{k=2}^{\infty} e^{-c}\frac{c^{k-1}}{(k-1)!}(k-1) = ce^{-c}\sum_{k=2}^{\infty}\frac{c^{k-2}}{(k-2)!} = c. \tag{A8}$$

Then in this case Eq. (A7) becomes

$$\left(\frac{I_1(\beta_c J)}{I_0(\beta_c J)}\right)(c) = 1. \tag{A9}$$

We stress that both critical conditions, Eqs. (A7) and (A9), can be obtained by expanding Eq. (11) around the PM solution [28,37]. In the ER case we see that the presence of nodes with a connectivity larger than c has the effect of lowering β_c, i.e., increasing T_c.

[1] J. Kosterlitz and D. Thouless, J. Phys. C **5**, L124 (1972).
[2] E. Brézin, J. Phys. (France) **43**, 15 (1982).
[3] E. Brézin, *Introduction to Statistical Field Theory* (Cambridge University Press, Cambridge, UK, 2010).
[4] J. Cardy, *Scaling and Renormalization in Statistical Physics* (Cambridge University Press, Cambridge, UK, 1996).
[5] Y. Kuramoto, Lect. Notes Phys. **39**, 420 (1975).
[6] J. A. Acebrón, L. L. Bonilla, C. J. Pérez Vicente, F. Ritort, and R. Spigler, Rev. Mod. Phys. **77**, 137 (2005).
[7] S. Gupta, A. Campa, and S. Ruffo, J. Stat. Mech. (2014) R08001.
[8] L. Angelani, C. Conti, L. Prignano, G. Ruocco, and F. Zamponi, Phys. Rev. B **76**, 064202 (2007).
[9] A. Gordon and B. Fischer, Phys. Rev. Lett. **89**, 103901 (2002).
[10] L. Angelani and G. Ruocco, Phys. Rev. E **76**, 051119 (2007).
[11] F. Antenucci, C. Conti, A. Crisanti, and L. Leuzzi, Phys. Rev. Lett. **114**, 043901 (2015).
[12] L. Angelani, C. Conti, G. Ruocco, and F. Zamponi, Phys. Rev. Lett. **96**, 065702 (2006).
[13] L. Leuzzi, C. Conti, V. Folli, L. Angelani, and G. Ruocco, Phys. Rev. Lett. **102**, 083901 (2009).
[14] C. Conti and L. Leuzzi, Phys. Rev. B **83**, 134204 (2011).
[15] F. Antenucci, M. Ibáñez Berganza, and L. Leuzzi, arXiv:1409.6345.
[16] H. Cao, Y. G. Zhao, S. T. Ho, E. W. Seelig, Q. H. Wang, and R. P. H. Chang, Phys. Rev. Lett. **82**, 2278 (1999).
[17] L. B. Soldano and E. C. M. Pennings, J. Lightwave Tech. **13**, 615 (1995).
[18] S. Jian and Z. Shi-Qun, Commun. Theor. Phys. **43**, 233 (2005).
[19] F. Rogister and R. Roy, Phys. Rev. Lett. **98**, 104101 (2007).
[20] M. Nixon, E. Ronen, A. A. Friesem, and N. Davidson, Phys. Rev. Lett. **110**, 184102 (2013).
[21] M. Sargent III, M. O'Scully, and W. E. Lamb, *Laser Physics* (Addison-Wesley, Reading, MA, 1978).
[22] H. A. Haus, *Waves and Fields in Optoelectronics* (Prentice-Hall, Englewood Cliffs, NJ, 1984).
[23] H. A. Haus, IEEE J. Quantum Electron. **6**, 1173 (2000).
[24] A. Gordon and B. Fischer, Opt. Commun. **223**, 151 (2003).
[25] M. Mézard and A. Montanari, *Information, Physics, and Computation* (Oxford University Press, New York, 2009).
[26] M. Mézard, G. Parisi, and M. A. Virasoro, *Spin Glass Theory and Beyond* (World Scientific, Singapore, 1987).
[27] M. Mézard and G. Parisi, Eur. J. Phys. B **20**, 217 (2001).
[28] C. Lupo and F. Ricci-Tersenghi (unpublished).
[29] M. Bellini and T. W. Hansch, Opt. Lett. **25**, 1049 (2000).
[30] T. Udem, R. Holzwarth, and T. Hansch, Nature **416**, 233 (2002).
[31] O. Svelto, *Principles of Lasers* (Springer-Verlag, Berlin, 1998).
[32] D. F. Nelson and W. S. Boyle, Appl. Opt. **1**, 181 (1962).
[33] N. M. Lawandy, R. M. Balachandran, A. S. L. Gomes, and E. Sauvain, Nature **368**, 436 (1994).
[34] H. Cao, J. Phys. A. : Math. Gen. **38**, 10497 (2005).
[35] D. S. Wiersma, Nat. Phys. **4**, 359 (2008).
[36] N. Ghofraniha, I. Viola, F. Di Maria, G. Barbarella, G. Gigli, L. Leuzzi, and C. Conti, Nat. Commun. **6**, 6058 (2015).
[37] N. S. Skantzos, I. P. Castillo, and J. P. L. Hatchett, Phys. Rev. E **72**, 066127 (2005).